

Session 3A5

Electromagnetic Modeling and Inversion and Applications 2

Compact LTCC BPF Design Using Lumped Elements	768
<i>J. W. Ha (Yonsei University, Korea); Y. J. Yoon (Yonsei University, Korea);</i>	
2.5D AGILD Electromagnetic Modeling and Inversion	769
<i>G. Xie (GL Geophysical Laboratory, USA); J. Li (, USA); F. Xie (GL Geophysical Laboratory, USA);</i>	
Measured Electromagnetic Pulses Verify Asymptotics and Analysis for Linear, Dispersive Media	774
<i>T. M. Roberts (Air Force Research Laboratory, USA);</i>	
Electromagnetic Modeling for Interpretation of Airborne SAR Imagery	778
<i>L. M. Zurk (Portland State University, USA); S. Matzner (Portland State University, USA); F. Farahbakhshian (Portland State University, USA); R. Toengi (Portland State University, USA);</i>	
Forward Problem Solution Using the Finite-difference Time-domain method combined with Frequency Scaling	779
<i>C. E. Vasios (Harvard Medical School, USA); L. M. Angelone (Harvard Medical School, USA); M. S. Hamalainen (Harvard Medical School, USA); J. W. Belliveau (Harvard Medical School, USA); G. Bonmassar (Harvard Medical School, USA);</i>	
Support Vector Machine Classification of Unexploded Ordnance Based on EMI Spheroidal Scattering Mode Coefficients	780
<i>B. J. Zhang (Massachusetts Institute of Technology, USA); K. O'Neill (Dartmouth College, USA); T. M. Grzegorzcyk (Massachusetts Institute of Technology, USA); J. A. Kong (Massachusetts Institute of Technology, USA);</i>	
Environmental Effects on UWB Electromagnetic Induction Inversion Techniques and Forward Modeling of Unexploded Ordnance	781
<i>B. J. Zhang (Massachusetts Institute of Technology, USA); K. O'Neill (Dartmouth College, USA); T. M. Grzegorzcyk (Massachusetts Institute of Technology, USA); J. A. Kong (Massachusetts Institute of Technology, USA);</i>	
Analysis of Uniplanar Resonator Using a Wave Concept Iterative Method W.C.I.P.	782
<i>N. Sboui (Faculté des Sciences de Tunis, Tunisia); A. Gharsallah (Faculté des Sciences de Tunis, Tunisia); A. Gharbi (Faculté des Sciences de Tunis, Tunisia); H. Baudrand (ENSEEHIT, France);</i>	
The KMD EMS System in Chinese Continuous Casting	783
<i>J. Li (Hunan Kemeid Mechanicsyco Ltd, China); Z. Q. Lai (Hunan Kemeid Mechanicsyco Ltd, China); J. H. Li (GL Geophysical Laboratory, USA); G. Q. Xie (GL Geophysical Laboratory, USA);</i>	
A New Formulation for Scattering by Impedant 3D Bodies	784
<i>B. Collard (Ecole nationale de l'Aviation Civile, France); B. Fares (Centre Europeen de Recherche et de Formation Avancee pour le Calcul Scientifique, France); B. Souny (Ecole nationale de l'Aviation Civile, France);</i>	

Compact LTCC BPF Design Using Lumped Elements

J. W. Ha and Y. J. Yoon
Yonsei University, Korea

In a filter design, it would be very useful if the orders of it can be reduced without sacrificing the passband response. Especially, it needs an efficient method to decrease the size of filter for the SDMB (Satellite Digital Mobile Broadcasting) in Korea. A low-order, which has a smaller circuit size, is suitable to SDMB device. Therefore, an effective method to design a BPF (Band Pass Filter) with a high skirt selectivity is presented in this paper. Each resonator is separated into inductor and capacitor region [1]. The proposed circuit merges the individual region. LTCC (Low Temperature Co-fired Ceramic) are used because it has the capability of high integration. The 3rd order BPF and the proposed circuits are shown in Fig. 1(a) and (b), respectively. The proposed circuit has fewer resonators than the conventional circuit. Consequently, the size of the proposed BPF is reduced to nearly 20% comparing with the typical 3rd order LTCC filters. The simulated and measured results are shown in Fig. 2. BPF with 3rd order resonator has the passband in SDMB band for -10 dB return loss and provides sufficient interference suppression in 2.4 GHz bluetooth band. Although the resonator is simplified in the modified circuit, it has enough bandwidth as well as stopband rolloff in the received channel. The measured results agree well with the simulation. Thus, it is found that the proposed circuit supports a compact BPF design. The additional process of design will be presented in the symposium.

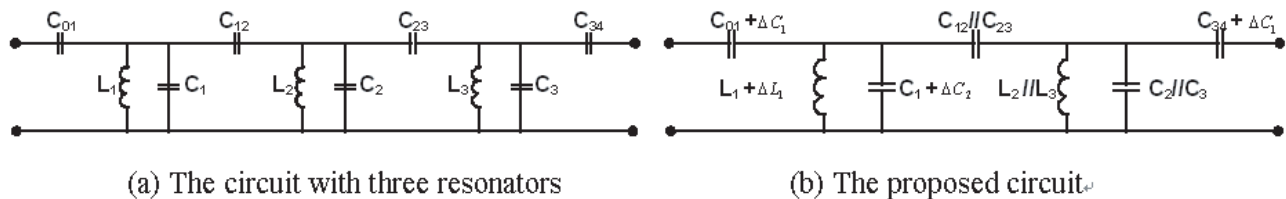


Figure 1: Circuits of BPF.

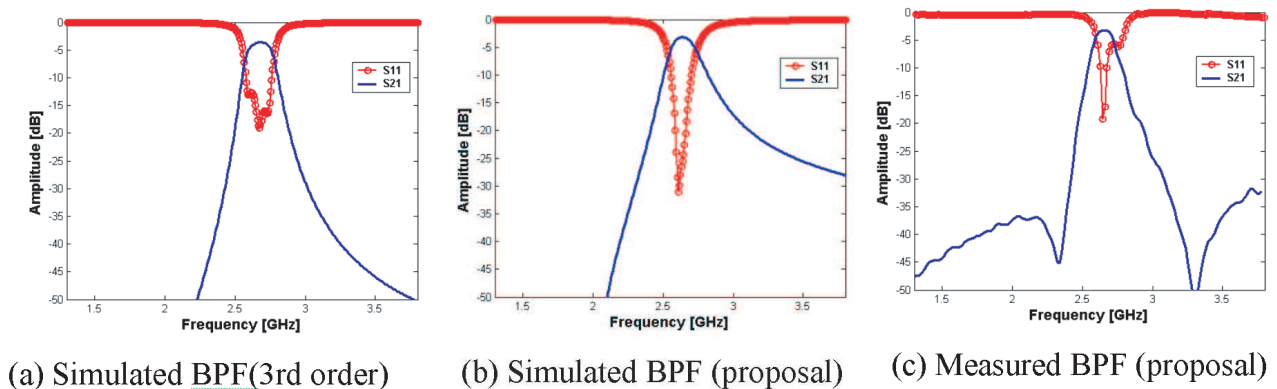


Figure 2: Comparison of simulated and measured results.

REFERENCES

1. Tang, C.-W., "Armonic-suppression LTCC filter with the step-impedance quarter-wavelength open stub," *IEEE Transactions on Microwave and Techniques*, Vol. 52, No. 2, Feb. 2004.

2.5D AGILD Electromagnetic Modeling and Inversion

G. Xie, J. Li, and F. Xie
GL Geophysical Laboratory, USA

Abstract—In this paper, we propose a new 2.5D AGILD electromagnetic (EM) modeling and inversion algorithms. We derive 2.5D differential integral equations for EM field on the boundary strip and center strip Ω_s with poles in cylindrical and spherical coordinate system. A 2.5D EM field Galerkin equation is derived on the remainder domain. It supposes that the electrical parameters in the rotational direction are uniform. In the cylindrical coordinate system, the EM field is function of the r , θ , and z . However, the electrical parameters are only depended on ρ and z . Upon substituting the Fourier series of the EM field into the strip differential integral equation and Galerkin equation, we propose the 2.5D AGILD EM modeling and inversion algorithm and develop its software. The 2.5D AGILD EM modeling and inversion algorithms and software are explained in the Figs.1–6. The AGILD method has the following advantages. (1) It vanishes error on the artificial boundary; (2) It reduces the full matrix and the ill posed for inversion; (3) It resolves coordinate singularities in cylindrical and spherical coordinate system in continuous castor, geophysics, singularities in north and south poles in Earth for EM field and Navier Stokes flow simulation in atmosphere; (4) AGILD has widely applications in geophysics, atmosphere, nano-materials, castor, medical, radio, motor, etc. areas; (5) The applications show that the 2.5D AGILD and GL are fast, accurate, and have reasonable high resolution.

1. Introduction

The Global Integral and Local Differential field modeling and parameter inversion GLID algorithms have been proposed since 1997 by Xie and Li [6–8]. The new AGILD EM modeling and inversion has been published in PIERS 2005 in Hangzhou and PIERS 2006 [1–5]. In this paper, we propose 2.5D AGILD EM modeling and inversion in cylindrical coordinate.

The AGILD modeling and inversion has widely applications for EM field and parameter in the motor and generator. They are useful for GEOMAIL, VEMP, cross hole imaging, MT, EM sheet, nanometer pipe and ball, blood pipe flow, MRI, medical instrument, microwave, coaxial antenna, and EM stirring, sensor, nondestructive testing etc. in the science and industrial engineering.

The arrangement of this paper is as follows: In the section 1, we have introduced 2.5D AGILD method and arranged our plan. In section 2, We propose the 2.5D EM differential integral equations. The 2.5D AGILD modeling algorithms are presented in the section 3. In section 4, we propose the 2.5D AGILD inversion. The Applications are described in the section 5. Finally, we present discussions and conclusion in the section 6.

2. The New 2.5D Em Differential Integral Equations

2.1. The 2.5D Em Differential Integral Equations

In the 2.5D EM modeling, the EM parameters σ , ε , and μ are independent on θ , and only variable in ρ and z . We choose the continuous component E_θ and H_θ to be unknown function. Upon substituting $[E, H] = \sum_{m=-\infty}^{\infty} [E_m, H_m](\rho, z)e^{im\theta}$ into the Maxwell equation in cylindrical coordinate, we derive the following 2.5D differential integral equations on the boundary strip and center strip domain containing pole $\rho = 0$, $E_{b\rho}^J, \dots, H_{bz}^M$ are known green tensor in the background medium, they are calculated in rectangle, cylindrical, and spherical coordinate system respectively.

$$\begin{aligned}
 & E_\theta(\rho', z', \theta'; \rho_s, z_s, \theta_s) - \int_{\partial\Omega^-} E_{b\rho}^J H_\theta \rho d\rho + E_{bz}^J H_\theta \rho dz - H_{b\rho}^J E_\theta \rho d\rho - H_{bz}^J E_\theta \rho dz \\
 & + \int_{\partial\Omega^-} E_\rho H_{b\theta}^J \rho d\rho + E_z H_{b\theta}^J \rho dz - H_\rho E_{b\theta}^J \rho d\rho - H_z E_{b\theta}^J \rho dz \\
 & - \int_{\Omega} (((\sigma_b + i\omega\varepsilon_b) - (\sigma + i\omega\varepsilon))(E_{b\rho}^J E_\rho + E_{bz}^J E_z - E_\theta E_{b\theta}^J)) \rho d\rho dz
 \end{aligned}$$

$$\begin{aligned}
& + \int_{\Omega} ((-i\omega\mu_b) - (-i\omega\mu))(H_{b\rho}^J H_{\rho} + H_{bz}^J H_z - H_{\theta} H_{b\theta}^J) \rho d\rho dz \\
= & \int_{\Omega} ((J_{\rho}) E_{\rho} + (J_z) E_z) \rho d\rho dz - \int_{\Omega} ((-i\omega\mu_b) M_{b\rho} H_{\rho} + (-i\omega\mu_b) M_{bz} H_z) \rho d\rho dz \\
& - \int_{\Omega} ((J_{\rho}) E_{b\rho}^J + (J_z) E_{bz}^J - J_{\theta} E_{b\theta}^J) \rho d\rho dz \\
& + \int_{\Omega} ((-i\omega\mu) M_{\rho} H_{b\rho}^J + (-i\omega\mu) M_z H_{bz}^J + (i\omega\mu) M_{\theta} H_{b\theta}^J) \rho d\rho dz \tag{1}
\end{aligned}$$

$$\begin{aligned}
& (-i\omega\mu_b) H_{\theta}(\rho', z', \theta'; \rho_s, z_s, \theta_s) + \int_{\partial\Omega-} E_{b\rho}^M H_{\theta} \rho d\rho + E_{bz}^M H_{\theta} \rho dz - H_{b\rho}^M E_{\theta} \rho d\rho - H_{bz}^M E_{\theta} \rho dz \\
& - \int_{\partial\Omega-} E_{\rho} H_{b\theta}^M \rho d\rho + E_z H_{b\theta}^M \rho dz - H_{\rho} E_{b\theta}^M \rho d\rho - H_z E_{b\theta}^M \rho dz \\
& + \int_{\Omega} (((\sigma_b + i\omega\varepsilon_b) - (\sigma + i\omega\varepsilon))(E_{b\rho}^M E_{\rho} + E_{bz}^M E_z - E_{\theta} E_{b\theta}^M)) \rho d\rho dz \\
& - \int_{\Omega} ((-i\omega\mu_b) - (-i\omega\mu))(H_{b\rho}^M H_{\rho} + H_{bz}^M H_z - H_{\theta} H_{b\theta}^M) \rho d\rho dz \\
= & - \int_{\Omega} ((J_{\rho}) E_{\rho} + (J_z) E_z) \rho d\rho dz + \int_{\Omega} ((-i\omega\mu_b) M_{b\rho} H_{\rho} + (-i\omega\mu_b) M_{bz} H_z) \rho d\rho dz \\
& + \int_{\Omega} ((J_{\rho}) E_{b\rho}^M + (J_z) E_{bz}^M - J_{\theta} E_{b\theta}^M) \rho d\rho dz \\
& - \int_{\Omega} ((-i\omega\mu) M_{\rho} H_{b\rho}^M + (-i\omega\mu) M_z H_{bz}^M - (-i\omega\mu) M_{\theta} H_{b\theta}^M) \rho d\rho dz \tag{2}
\end{aligned}$$

where the E_{ρ} , E_z , H_{ρ} , and H_z will be represented by E_{θ} , H_{θ} in the Eqs. (1) and (2).

2.2. The 2.5 D EM Garlekin Equation in the Cylindrical System

Upon substituting Fourier series $[E, H] = \sum_{m=-\infty}^{\infty} [E_m, H_m](\rho, z) e^{im\theta}$ into the Maxwell equation in cylindrical coordinate, let E_{θ} , H_{θ} denote $E_{\theta m}$, $H_{\theta m}$, we derive the following 2.5 D EM Garlekin equation,

$$\begin{aligned}
& \int_{\Omega} \frac{\rho^2}{(k^2\rho^2 - m^2)} \left(\left(\frac{1}{\rho} im \frac{\partial H_{\theta}}{\partial z} + (\sigma + i\omega\varepsilon) \frac{1}{\rho} \frac{\partial \rho E_{\theta}}{\partial \rho} \right) \frac{1}{\rho} \frac{\partial \rho \phi}{\partial \rho} - \left(\frac{1}{\rho} im \frac{1}{\rho} \frac{\partial \rho H_{\theta}}{\partial \rho} - (\sigma + i\omega\varepsilon) \frac{\partial E_{\theta}}{\partial z} \right) \frac{\partial \phi}{\partial z} \right) \rho d\rho dz \\
& - \oint_{\partial\Omega} \frac{\rho^2}{(k^2\rho^2 - m^2)} \left(\left(\frac{1}{\rho} im \frac{\partial H_{\theta}}{\partial z} + (\sigma + i\omega\varepsilon) \frac{1}{\rho} \frac{\partial \rho E_{\theta}}{\partial \rho} \right) \rho \phi dz + \left(\frac{1}{\rho} im \frac{1}{\rho} \frac{\partial \rho H_{\theta}}{\partial \rho} - (\sigma + i\omega\varepsilon) \frac{\partial E_{\theta}}{\partial z} \right) \rho \phi d\rho \right), \\
= & - \int_{\Omega} \frac{\rho^2}{(k^2\rho^2 - m^2)} \left(\left(\frac{1}{\rho} im (J_z) + (k^2) M_{\rho} \right) \frac{\partial \phi}{\partial z} + \left(\frac{1}{\rho} im J_{\rho} - k^2 M_z \right) \frac{1}{\rho} \frac{\partial \rho \phi}{\partial \rho} \right) \rho d\rho dz \\
& + \int_{\Omega} ((\sigma + i\omega\varepsilon)(E_{\theta} + J_{\theta}) \rho \phi d\rho dz + \oint_{\partial\Omega} \frac{\rho^2}{(k^2\rho^2 - m^2)} \left(\left(\frac{1}{\rho} im J_{\rho} - k^2 M_z \right) \rho \phi dz - \left(\frac{1}{\rho} im (J_z) + (k^2) M_{\rho} \right) \rho \phi d\rho \right), \tag{3}
\end{aligned}$$

$$\begin{aligned}
& \int_{\Omega} \frac{\rho^2}{(k^2\rho^2 - m^2)} \left(\left(\frac{1}{\rho} im \frac{\partial E_{\theta}}{\partial z} + (-i\omega\mu) \frac{1}{\rho} \frac{\partial \rho H_{\theta}}{\partial \rho} \right) \frac{1}{\rho} \frac{\partial(\phi\rho)}{\partial \rho} - \left(\frac{1}{\rho} im \frac{1}{\rho} \frac{\partial \rho E_{\theta}}{\partial \rho} - (-i\omega\mu) \frac{\partial H_{\theta}}{\partial z} \right) \frac{\partial \phi}{\partial z} \right) \rho d\rho dz, \\
& - \oint_{\partial\Omega} \frac{\rho^2}{(k^2\rho^2 - m^2)} \left(\left(\frac{1}{\rho} im \frac{\partial E_{\theta}}{\partial z} + (-i\omega\mu) \frac{1}{\rho} \frac{\partial \rho H_{\theta}}{\partial \rho} \right) \phi \rho dz + \left(\frac{1}{\rho} im \frac{1}{\rho} \frac{\partial \rho E_{\theta}}{\partial \rho} - (-i\omega\mu) \frac{\partial H_{\theta}}{\partial z} \right) \phi \rho d\rho \right) \\
& = \int_{\Omega} \frac{\rho^2(-i\omega\mu)}{(k^2\rho^2 - m^2)} \left(\left(-\frac{1}{\rho} im M_z - J_{\rho} \right) \frac{\partial \phi}{\partial z} - \left(\frac{1}{\rho} im M_{\rho} - J_z \right) \frac{1}{\rho} \frac{\partial(\phi\rho)}{\partial \rho} \right) \rho d\rho dz \\
& + \int_{\Omega} (-i\omega\mu)(H_{\theta} + M_{\theta})\phi \rho d\rho dz + \oint_{\partial\Omega} \frac{\rho^2(-i\omega\mu)}{(k^2\rho^2 - m^2)} \left(\left(\frac{1}{\rho} im M_{\rho} - J_z \right) \phi \rho dz + \left(-\frac{1}{\rho} im M_z - J_{\rho} \right) \phi \rho d\rho \right), \quad (4)
\end{aligned}$$

where function ϕ is test function. When $m = 0$, the Eqs. (3) and (4) have singularity in the pole $\rho = 0$. The traditional FEM and FD method have singularity in the pole $\rho = 0$.

3. The New 2.5 D AGILD Modeling

Fortunately, our 2.5D differential integral Eqs. (1) and (2) have no coordinate singularity in the pole $\rho = 0$. We use collocation FEM points to discrete the Eqs. (1) and (2) on the boundary strip and center strip containing the pole point $\rho = 0$. The double layered discrete matrix equation is as follows

$$K_{BB} \begin{bmatrix} E_{\theta B_y} \\ H_{\theta B_y} \end{bmatrix} + K_{BI} \begin{bmatrix} E_{\theta I_y} \\ H_{\theta I_y} \end{bmatrix} = \begin{bmatrix} J_{sB} \\ M_{sB} \end{bmatrix} \quad (5)$$

where $[E_{\theta B}, H_{\theta B}]$ is the θ component EM field on the external layer of the center strip and boundary strip, $[E_{\theta I}, H_{\theta I}]$ is the θ component EM field on the internal layer of the center boundary strip. $[J_{sB}, M_{sB}]$ is the discrete source term on the boundary and center strip, On the remainder domain which has no pole point, we use Garlekin FEM to discrete the 2.5 D EM Garlekin Eqs. (3) and (4) and get sparse matrix equation. By GILD processes from internal to external, we obtain

$$K_{IB} \begin{bmatrix} E_{\theta B_y} \\ H_{\theta B_y} \end{bmatrix} + K_{II} \begin{bmatrix} E_{\theta I_y} \\ H_{\theta I_y} \end{bmatrix} = \begin{bmatrix} J_{sI} \\ M_{sI} \end{bmatrix}, \quad (6)$$

where $[J_{sI}, M_{sI}]$ is the composed source term in the internal layered. By solving the coupled Eqs. (5) and (6), we obtain $[E_{\theta B}, H_{\theta B}]$ and $[E_{\theta I}, H_{\theta I}]$. Using backward processes, we obtain $[E_{\theta}, H_{\theta}]$ in the whole domain for each m sheet (see Figure).

Because the Garlekin FEM (6) is build on the domain without singularity pole, and the differential integral discrete Eq. (5) has no coordinate singularity, Therefore, Our 2.5D AGILD method resolve the coordinate singularity historical difficulty.

4. The New 2D AGILD Inversion

In the 2.5D AGILD EM modeling, we suppose the EM parameter is invariable in the θ . The EM parameters are variable in the ρ and z of 2D. We present the 2D AGILD inversion here.

4.1. Variance EM Differential Integral Equation

We propose the 2.5D EM variation differential integral equation on the strip for inversion

$$\begin{aligned}
 & \delta E_{\theta}(\rho', z', \theta'; \rho_s, z_s, \theta_s) - \delta \int_{\partial\Omega^-} E_{b\rho}^J H_{\theta} \rho d\rho + E_{bz}^J H_{\theta} \rho dz - H_{b\rho}^J E_{\theta} \rho d\rho - H_{bz}^J E_{\theta} \rho dz \\
 & + \delta \int_{\partial\Omega^-} E_{\rho} H_{b\theta}^J \rho d\rho + E_z H_{b\theta}^J \rho dz - H_{\rho} E_{b\theta}^J \rho d\rho - H_z E_{b\theta}^J \rho dz \\
 & = \int_{\Omega} \delta(\sigma + i\omega\varepsilon)(E_{b\rho}^J E_{\rho} + E_{bz}^J E_z - E_{\theta} E_{b\theta}^J) \rho d\rho dz \\
 & - \int_{\Omega} \delta(-i\omega\mu)(H_{b\rho}^J H_{\rho} + H_{bz}^J H_z - H_{\theta} H_{b\theta}^J) \rho d\rho dz \\
 & = \delta \int_{\Omega} (J_{\rho} E_{\rho} + J_z E_z) \rho d\rho dz - \delta \int_{\Omega} ((-i\omega\mu_b) M_{b\rho} H_{\rho} + (-i\omega\mu_b) M_{bz} H_z) \rho d\rho dz \\
 & + \delta \int_{\Omega} ((-i\omega\mu) M_{\rho} H_{b\rho}^J + (-i\omega\mu) M_z H_{bz}^J + (i\omega\mu) M_{\theta} H_{b\theta}^J) \rho d\rho dz, \tag{7}
 \end{aligned}$$

$$\delta E_z = \frac{-2k\delta k\rho^2}{(k^2\rho^2 - m^2)^2} \left(\frac{1}{\rho} im \frac{\partial E_{\theta}}{\partial z} + (-i\omega\delta\mu) \frac{1}{\rho} \frac{\partial \rho H_{\theta}}{\partial \rho} + (-i\omega\delta\mu) \frac{1}{\rho} im M_{\rho} - (-i\omega\delta\mu)(J_z) \right), \tag{8}$$

Similarly, we can derive the variance of δE and δH . Also, we can derive the variance equation of the differential integral Eq. (2), and Gerlekin Eqs. (3) and (4).

4.2. Discrete Variance Em Differential Integral Equation

By using collocation FEM discretization of the variance EM differential integral equations, and regularizing with parameter and linearization, the matrix equation of the (7) relative $[\delta\sigma, \delta\varepsilon, \delta\mu]_{B_s}$ in boundary strip to $[\delta\sigma, \delta\varepsilon, \delta\mu]_{i_s}$ in inside strip will be

$$\mathfrak{S}_{\mathbf{B}_s B_s} \begin{bmatrix} \delta\sigma_{B_s} \\ \delta\varepsilon_{B_s} \\ \delta\mu_{B_s} \end{bmatrix} + \mathfrak{S}_{B_s I_s} \begin{bmatrix} \delta\sigma_{I_s} \\ \delta\varepsilon_{I_s} \\ \delta\mu_{I_s} \end{bmatrix} = \begin{bmatrix} \delta E_{\theta} \\ \delta H_{\theta} \end{bmatrix}_{D_s}, \tag{9}$$

and using EM discretization of the variance Gerlekin equation and weaker regularizing linearization, we obtain matrix equation relative $[\delta\sigma, \delta\varepsilon, \delta\mu]_{i_s}$ in inside strip to $[\delta\sigma, \delta\varepsilon, \delta\mu]_{B_s}$ in boundary strip. By solving the coupled matrix equation and backward processes, we obtain the variance of the EM parameter $[\delta\sigma, \delta\varepsilon, \delta\mu]$ that is used to update the parameter. The 2.5D AGILD EM modeling and inversion are explained by Figs. 1-6.

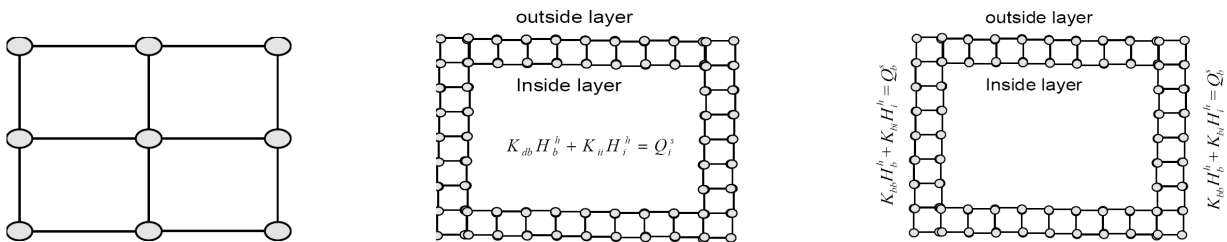


Fig. 1: AGILD forward node scheme. Fig. 2: Inside node layer to outside layer. Fig. 3: Outside node layer to inside layer.

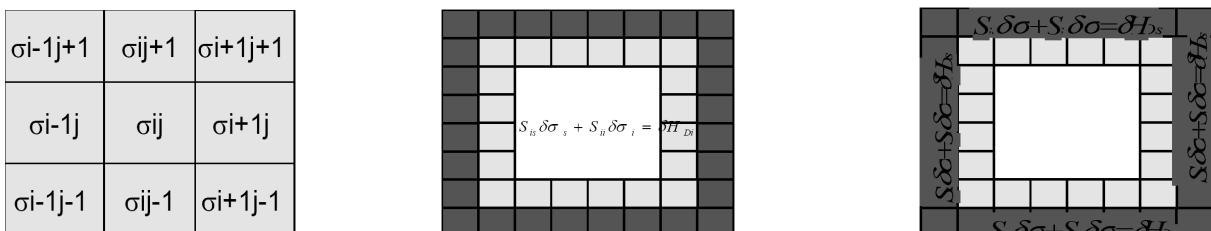


Fig. 4: AGILD inverse block scheme. Fig. 5: Inside block layer to outside layer. Fig. 6: Outside block layer to inside layer.

5. The Applications

The 2.5D AGILD modeling and inversion have widely applications in GEOMAIL, VEMP, EM sheet, cross hole imaging etc. geophysical exploration, Earthquake exploration, coaxial antenna, motors and generators design, EM stirring in caster, microwave cell phone design, environment, EM in nanometer pipe and ball, sensor design, nondestructive testing. AGILDMAIL, AGILDVEMP, AGILDSheet, and ADILDEMS [5] etc software have been developed. The Earth sphere magnetic field is simulating. 2.5D AGILD can be parallelization by using frequency f_i , wave number k_{zj} and angle number θ_m . Many GL [2] and AGILD results are publishing in Journals.

6. Discussions and Conclusion

Many synthetic and field data imaging show that AGILD method is fast and accurate without any boundary error reflection, and AGILD inversion is high resolution. 2.5 AGILD has same merits as AGILD and GILD. Its main merits are (1) to reduce cost to 2D, (2) vanish error boundary reflection, and resolve singularities in cylindrical and spherical coordinate.

REFERENCES

1. Xie, G. Q., J. H. Li, and F. Xie, "Advanced GILD EM modeling and inversion," *Proc. PIERS*, Hangzhou, 105.
2. Xie, G., F. Xie, and J. Li, "New GL method and its advantages for resolving historical difficulties," *PIERS 2006*.
3. Xie, G. Q., J. H. Li, and F. Xie, "AGILD geophysical and atmosphere imaging, in preparation."
4. Li, J., G. Xie, and F. Xie, "New stochastic AGILD EM modeling and inversion," *Piers 2006*, Cambridge.
5. Li, J., G. Xie, and J. Li, "2.5D AGLID EMS Stirring modeling in the cylindrical coordinate," *Piers 2006*.
6. Xie, G. and J. Li, "New parallel SGILD modeling and inversion," *Physics D*, Vol. 133, 477–487, 1999.
7. Xie, G., J. Li, D. Zuo, E. Majer, and M. Oristaglio, "3-D electromagnetic modeling and nonlinear inversion," *Geophysics*, Vol. 65, No. 3, 804–822, 2000.
8. Xie, G. and J. Li, "A new algorithm for 3D nonlinear EM inversion," *3D Electromagnetics Book*, 193, 1995.

Measured Electromagnetic Pulses Verify Asymptotics and Analysis for Linear, Dispersive Media

T. M. Roberts

Air Force Research Laboratory, USA

Abstract—Electromagnetic precursors and other pulses in dispersive media have been studied theoretically since 1914. Yet a recent National Research Council study [1, p. 73–75] found few measurements that verify the relevant theories. Verification is useful because, where independent theories and measurements agree, the results are highly reliable. This report describes two laboratory verifications of transient-electromagnetic theory that I completed recently.

1. Introduction

Laboratory measurements of dc-content, electromagnetic pulses verify two groups' asymptotics for the dispersive decay and spread of pulses in a Debye model and the spread in a Lorentz model [2]. The measured peak amplitudes of pulses decay with depth nearly as $x^{-1/2}$ (water) and $x^{-1/3}$ (concrete) in coaxial cables. The products of the measured peaks and full-widths at half-maximum (FWHMs) are nearly constant. This was predicted for water and for all Debye models; for concrete, it was a surprise.

Other, independent measurements verify analysis showing that any pulse decays exponentially in a lossy material if the pulse's spectrum has nonzero separation from $\omega = 0$ (dc) [3–5]. The energy and peak amplitude then decay at least as fast as their respective slowest rates of exponential decay for the material and spectrum at hand. By basic antenna theory, frequencies near dc have infinitesimal efficiency of radiating into the far field [3]. Thus, exponential decay is nearly universal in far-field, lossy objects.

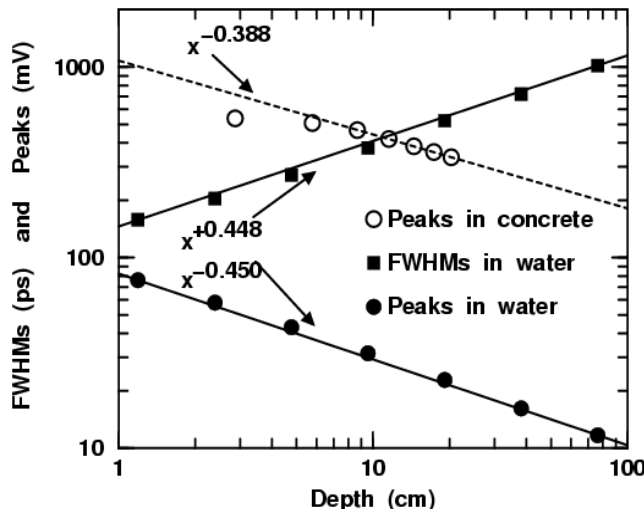


Figure 1: Peaks $\propto x^{-0.450}$ and FWHMs $\propto x^{-0.448}$ for $x > 1$ cm in water. Peaks $\propto x^{-0.388}$ for $x > 8$ cm in concrete.

2. Verification of Debye- and Lorentz-model Asymptotics

Petropoulos and I showed that the Dirac $\delta(t)$ response of any Debye model will asymptotically approach the δ response of an advection-diffusion equation as the depth x greatly exceeds an easily computed quantity that we named the time-domain skin depth [6]. As $x \rightarrow \infty$, the δ response's peak amplitudes decay as $x^{-1/2}$ and the full widths at half-maximum (FWHMs) spread as $x^{1/2}$ in Debye models. Some of these results, and further results, were obtained independently by Kelbert and Sazonov [7, secs. 2.2 and 2.3] in the same year (1996) as [6]. In mid-1997, Farr and Frost published relevant experimental data for water and concrete [8]. Because the three groups were unaware of each other's work, the results were profoundly independent.

A theorem on “element convolution” [6] predicted that Farr and Frost’s measured pulse would propagate in a Debye model of water with peaks $\propto x^{-1/2}$ and FWHMs $\propto x^{1/2}$, approximately [2]. This is evident in Fig. 1, where peaks \times FWHMs are constant to within $\pm 1.4\%$ for water, verifying much of the three groups’ work. For concrete, peaks \times FWHMs are constant to within $\pm 6.2\%$ but the reason is not known.

Debye models are not good for concrete. But Farr and Frost’s best Lorentz model for concrete is a good fit for the real part of the complex permittivity, $\varepsilon(\omega)$. Unfortunately, the same Lorentz-model fit badly understates $\text{Im } \varepsilon$, typical of Lorentz-model fits for solids [9, ch. 3, sec. 2.2 and 2.3]. Even in these circumstances, a derivation [2, sec. IV] shows that the pulse’s measured FWHM would be well accounted for by asymptotics for the Lorentz model, provided the asymptotics themselves are good.

One basic test of Lorentz-model asymptotics is that, as $x \rightarrow \infty$, the peak amplitude of any propagated pulse decays asymptotically as $x^{-1/3}$ if the incident pulse’s Fourier transform, $\tilde{f}(\omega)$, is nonzero at $\omega = 0$; but the decay is $x^{-2/3}$ if \tilde{f} has a first-order zero at $\omega = 0$ [6, endnote 30]. This basic test has precedence in Brillouin’s $x^{-1/3}$ revision, in 1932, of his incorrect $x^{-1/2}$ Lorentz-model result from 1914; albeit for only one variety of incident pulse [10, p. 105–110, 124–127]. Some more-recently-published Lorentz-model asymptotics [11, paragraph 2 of p. 352] fail the basic test. Kelbert and Sazonov’s asymptotics [7, sec. IV] pass the test.

Kelbert and Sazonov’s asymptotics accommodate Farr and Frost’s Lorentz-model fit and their incident pulse for concrete. The result is Fig. 2, which shows reasonably good agreement of theory and the FWHMs measured beyond 6 cm in concrete.

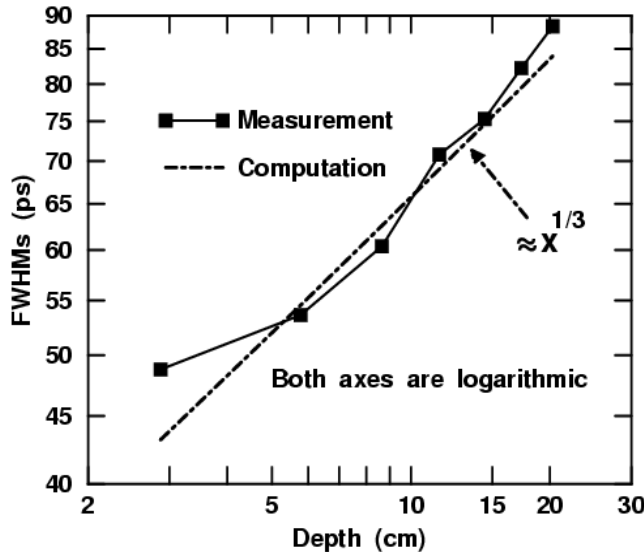


Figure 2: Measured and theoretical FWHMs agree for $x > 6$ cm in concrete.

In this manner, one measurement group (Farr and Frost) and two theory groups (Kelbert and Sazonov, and Petropoulos and me) published mutually verifying results within nearly a year of each other, without even knowing of each other. The mutual verifications include both the Debye and Lorentz models. The verification for Lorentz-model asymptotics is partial—valid for only FWHMs—because Lorentz models typically understate the $\text{Im } \varepsilon$ of solids [9].

3. Verification of Exponential Decay

From 1914 [10] until July 4, 2002 [3], apparently, almost every pulse-decay rate predicted for a dispersion model was of the form $x^{-\text{const}}$, called algebraic decay. Decay rates are sensitive to the degree of spectral concentration near $\omega = 0$ (dc) [6, endnote 30]. What happens if an incident pulse’s spectrum is confined to a non-infinite band of frequencies separated by a nonzero amount from dc, as broadcast regulations and practicality may require? The frequency components still would travel as $\exp(ikx)$, where $k(\omega)$ is the complex-valued wave number. Let k_i^{\min} be the smallest positive value that $\text{Im } k$ has for the material and spectrum at hand. Intuition then suggests that the full pulse’s peak would decay at least as fast as the slowest rate of exponential decay, $\exp(-k_i^{\min}x)$.

Exponential-decay derivations [12] are suitable for undergraduate textbooks. Let $\bar{\mathcal{E}}(x) = \mathcal{E}(x)/\mathcal{E}(0)$ be the normalized energy, where $\mathcal{E}(x) = \int_{-\infty}^{\infty} |E(x,t)|^2 dt$. Incident pulses $f(t)$ with Fourier transforms $\tilde{f}(\omega)$ propagate linearly as $E(x,t) = \int_{-\infty}^{\infty} e^{i[k(\omega)x + \omega t]} \tilde{f}(\omega) d\omega$. The Parseval equation then implies $\int_{-\infty}^{\infty} |E(x,t)|^2 dt = \int_{-\infty}^{\infty} |e^{ikx} \tilde{f}(\omega)|^2 d\omega$ and algebra shows $\bar{\mathcal{E}}(x) \leq \int_{-\infty}^{\infty} e^{-2k_i^{\min} x} |\tilde{f}(\omega)|^2 d\omega = e^{-2k_i^{\min} x} \int_{-\infty}^{\infty} |\tilde{f}|^2 d\omega = e^{-2k_i^{\min} x} \int_{-\infty}^{\infty} f^2 dt$. The value k_i^{\min} is defined in the previous paragraph.

A similar, 5-step derivation [3,12] proves the exponential decay of normalized peak amplitudes, $\bar{\mathcal{P}}(x) = \mathcal{P}(x)/\mathcal{P}(0)$, where $\mathcal{P}(x) \equiv \max_t |E(x,t)|$. In fact, $\bar{\mathcal{P}}(x) \leq e^{-2k_i^{\min} x} \int_{-\infty}^{\infty} |\tilde{f}| d\omega$. This relation for peaks was verified in 2002 by a 4-parameter, infinite family of numerical examples [3] for the Debye and Lorentz models.

Two years after the exponential decay of $\bar{\mathcal{P}}$ was verified numerically, the exponential decay of $\bar{\mathcal{E}}$ was verified experimentally [4, 5]. The experiment is described next.

Choi and Österberg measured $\bar{\mathcal{E}}(x)$ for a 660–740-nm-wavelength red laser pulse traveling 4.7 m in deionized water [4]. Their explicit motivation was to observe a pulse that decays slower than exponentially.

Choi and Österberg's data analysis yielded a graph [4, Fig. 1] that their concluding paragraph used as evidence of $\approx x^{-1/2}$ decay of $\bar{\mathcal{E}}(x)$. The evidence was weak: The $x^{-1/2}$ claim was based on only the last 4 of 24 data points. The error bars along a *logarithmic* axis were centered on the data and had constant lengths, without explanation for the cause. The dotted curve for $\exp(-2k_i^{\min} x)$ was mislabeled. And the k_i^{\min} value used in [4] represented the experiment's *deionized water* by this uncommon mixture: 25% Sargasso Sea water; $\approx 25\%$ water from Crater Lake National Park, USA; and $\approx 50\%$ doubly-distilled water [5, paragraph 3]. Sea water, especially, is unlike the deionized water used experimentally in [4].

Figure 3 is adapted from [5]. It corrects [4, Fig. 1]. The experiment's deionized water is represented here by the k_i^{\min} value for twice-distilled water at the 660 nm wavelength. The measurements of normalized energy $\bar{\mathcal{E}}(x)$ are marked. Fig. 3 shows that these measurements decay exponentially, as $\bar{\mathcal{E}}(x) \leq \exp(-2k_i^{\min} x)$, for 24 data points whose 0.001–4.7 m span covers 3.7 decades of depth. Please notice how close the measured data are to the theoretically slowest rate of decay (solid curve) for the material and spectrum at hand.

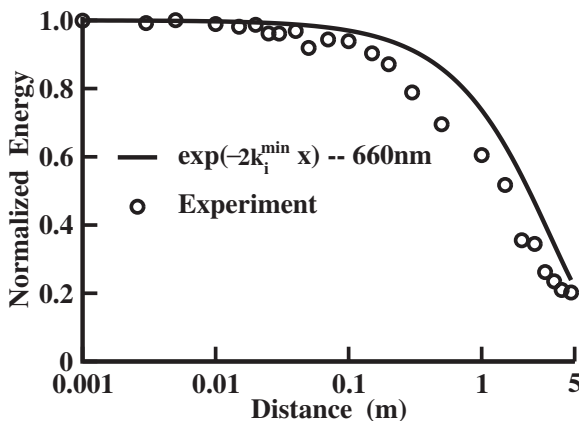


Figure 3: Experimental verification of the exponential decay of $\bar{\mathcal{E}}(x)$, showing each datum in 3.7 decades of distance.

4. Conclusion

Studies of 1D electromagnetic pulses in dispersion models date to 1914 [10]. For the next 88 years, apparently, it was largely unnoticed that many pulses used in that theory could not propagate into the far field because they had dc ($\omega = 0$) content. Such pulses can travel in waveguides with dispersive fill, but few such measurements existed until recently [1, p. 73–75]. Quantitative agreement of measurement and theory has since improved by means mentioned in sec. 2, which regards pulses with dc in the spectrum or at a spectral endpoint.

When a 1D pulse's spectrum is separated from dc by a nonzero amount, the pulse will decay exponentially in lossy materials. The relevant measurements and derivations here in sec. 3 and in [4, 5, 12] seem suitable for the undergraduate curriculum in electromagnetics.

Acknowledgment

This work was supported by the U.S. Air Force Office of Scientific Research/NM.

REFERENCES

1. Barnes, F. S., et al., "An assessment of potential health effects from exposure to PAVE PAWS low-level phased-array radiofrequency energy," National Academy of Sciences, Washington DC, 2005. Available from <http://books.nap.edu/catalog/11205.html> (click "... Download").
2. Roberts, T. M., "Measured and predicted behavior of pulses in Debye- and Lorentz-type materials," *IEEE Trans. Antennas Propag.*, Vol. 52, No. 1, 310–314, 2004.
3. Roberts, T. M., "Radiated pulses decay exponentially in the far-fields of antennas," *Electron. Lett.*, Vol. 38, No. 14, 679–680, 2002.
4. Choi, S.-H. and U. Österberg, "Observation of optical precursors in water," *Phys. Rev. Lett.*, Vol. 92, No. 19, 193903, 2004.
5. Roberts, T. M., "Comment on 'Observation of optical precursors in water'," *Phys. Rev. Lett.*, Vol. 93, No. 26, 269401, 2004.
6. Roberts, T. M. and P. G. Petropoulos, "Asymptotics and energy estimates for electromagnetic pulses in dispersive media," *J. Opt. Soc. Amer. A*, Vol. 13, No. 6, 1204–1217, 1996; —, *Addendum*, Vol. 16, No. 11, 2799–2800, 1999.
7. Kelbert, M. and I. Sazonov, *Pulses and Other Wave Processes in Fluids*, Kluwer, Dordrecht, The Netherlands, 1996.
8. Farr, E. G. and C. A. Frost, "Ultra-wideband antennas and propagation," U.S. Air Force Tech. Rep. [4 Vols.], 1997. Available from <http://handle.dtic.mil/100.2/ADA328785>, ADA328 786, ADA328 787, and ADA328 788.
9. Fox, M., *Optical Properties of Solids*, Oxford University Press, Oxford, UK, 2001.
10. Brillouin, L., *Wave Propagation and Group Velocity*, Academic Press, San Diego, 1960.
11. Oughstun, K. E. and G. C. Sherman, *Electromagnetic Pulse Propagation in Causal Dielectrics*, Springer-Verlag, Heidelberg, Germany, 1994.
12. Roberts, T., "PAVE PAWS radiation decays exponentially in lossy materials," U.S. Air Force Tech. Rep. ADA411823, 2002. Available from <http://handle.dtic.mil/100.2/ADA411823>. See p. 11–15, Eq. 1 of p. 51, and p. 52.

Electromagnetic Modeling for Interpretation of Airborne SAR Imagery

L. M. Zurk, S. Matzner, F. Farahbakhshian, and R. Toengi
Portland State University, USA

The theory that governs the formation of Synthetic Aperture Radar (SAR) imagery generally assumes that the radar return is due to stationary, isolated, and uncorrelated point scatterers distributed on a flat plane. For most naturally occurring scenes (such as those arising in remote sensing applications) this assumption does not apply. This lack of consideration for the electromagnetic scattering phenomenology limits the useful interpretation of the SAR imagery, and places the burden of recognizing image features on the expertise of the image analyst. In this work, an end-to-end electromagnetic and radar simulation model has been developed to understand and evaluate the appearance of complicated scene features in spotlight SAR images as a function of scene parameters, sensor characteristics, and radar processing approaches. Furthermore, the model can be employed to investigate the potential of advanced physics-based processing techniques that can be used to produce more appropriately-formed image output.

The model uses as input Digital Terrain Elevation Data (DTED) with accompanying information on land cover and/or building structures. The scattering from the terrain is computed using a modified Kirchoff scattering approximation, where the modification takes into account local terrain slopes. The surface roughness is assumed to have a Gaussian distribution with the RMS height and correlation length chosen as appropriate for the specified class of land cover. The scattering model has been developed to emulate the performance of the Lincoln Multi-Mission ISR Testbed (LiMIT). LiMIT is an airborne SAR sensor that was developed and deployed by MIT Lincoln Laboratory, with a recent collection campaign over San Clemente Island as part of the Navy's Silent Hammer Sea Trial experiment. In this talk, an initial comparison of the output imagery of the SAR synthesis model is compared to images acquired by LiMIT during Silent Hammer. Further extensions to the model and concepts for physics-based SAR processing will be presented and discussed.

Forward Problem Solution Using the Finite-difference Time-domain method combined with Frequency Scaling

C. E. Vasios, L. M. Angelone, M. S. Hamalainen, J. W. Belliveau, and G. Bonmassar
Harvard Medical School, USA

INTRODUCTION: The estimation of sources underlying measured MEG and EEG signals requires an accurate solution of the static approximation of Maxwell's equations that can be conveniently expressed as the lead field [1], which is the sensitivity distribution of a given MEG sensor or an EEG electrode. In the present state-of-the-art approach for lead field estimation (Boundary Element Method, BEM) [2] the head is described with a few compartments with constant and isotropic electrical conductivity. Arbitrary, anisotropic conductivity distributions can be handled with the finite-element and finite-difference methods. This allows taking into consideration thin and highly conductive tissues such as bone marrow, disregarded when using the BEM. We propose a new approach for the lead field computation using the cell-oriented finite-difference time-domain (FDTD) method combined with the frequency scaling technique [3] for low frequencies.

METHODS:

Head Model and Electrode Locations: One 29-tissue high-resolution (1 mm^3) head model (Fig. 1) segmented from the anatomical MRI data was used (a 6 mm^3 resolution was used here). The tissue conductivities were selected according to the literature [4].

We computed the lead field from 32 electrode locations (digitized from a real EEG recording) on this particular subject which we co-registered to the head model and used the 33rd electrode near the vertex (Cz) as a reference.

Lead Field Computation: The reciprocity theorem states that the lead field of a given electrode pair is the same as the current pattern generated in the underlying conductor by feeding a unit current through the electrodes. Therefore, we were able to apply the FDTD method to calculate induced current densities using XFDTD software (REMCOM Co.). For dramatical reduction of computational time, simulations at target frequency $f = 20\text{ Hz}$ were initially performed at a higher frequency $f' = 20\text{ MHz}$ and then scaled, $J(f) = (f/f')J(f')$, according to the frequency scaling technique [3].

RESULTS-CONCLUSIONS: The comparison of the results from the FDTD computation with those given by a three-compartment boundary-element model showed that the lead field distributions are qualitatively similar. The computation of the lead field for one electrode pair took about 80 minutes on a 2-processor desktop computer (Intel XEON 2.8 GHz, 2 GB RAM).

FDTD can incorporate an arbitrary conductivity distribution and anisotropy without the need of complex meshing techniques typically needed in the finite-element and BEM approaches.

REFERENCES

1. Wolters, C. H., et al., *Inverse Problems*, Institute of Physics Publishing, Vol. 20, 1099–1116, 2004.
2. Oostendorp, T. F., et al., *IEEE Trans. on Biomed. Eng.*, Vol. 36, No. 3, 382–391, 1989.
3. Moerlose, J., et al., *Radio Science*, Vol. 32, No. 2, 329–341, 1997.
4. Gabriel, C., Brooks Air Force Technical Report AL/OE-TR-1996-0037.

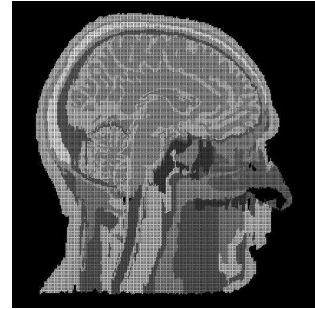


Figure 1: Anatomically accurate $1 \times 1 \times 1\text{ mm}^3$ resolution head model used for induced currents simulations.



Figure 2: Induced current densities computed after connecting Cz and T8 positions with a current source of 1 A.

Support Vector Machine Classification of Unexploded Ordnance Based on EMI Spheroidal Scattering Mode Coefficients

B. J. Zhang

Massachusetts Institute of Technology, USA

K. O'Neill

Dartmouth College, USA

T. M. Grzegorzczuk and J. A. Kong

Massachusetts Institute of Technology, USA

This project developed discrimination techniques that might be applied to distinguish unexploded ordnance (UXO) from large clutter pieces using their frequency domain UWB electromagnetic induction (EMI) response measurements. We use a forward scattering model for spheroids to represent UXO because they are typically elongated bodies of revolution. Our forward model describes the EMI response of objects in terms of spheroidal excitation and scattering modes. The coefficients of the scattering modes have been shown to be unique for a given scattering response. Therefore, we use the coefficients of the spheroidal scattering modes as inputs into a support vector machine (SVM), a binary classification algorithm based on statistical learning. We train the SVM by presenting it with the scattering coefficients of objects in known classes. Then, new objects with unknown class can be correctly classified by a trained SVM through analysis of their spheroidal scattering mode coefficients. Previous studies have shown that this approach to classification of similar objects on the basis of object elongation and magnetic permeability is achievable with a high degree of accuracy. Our current study focuses on scatterer volume because the amount of metal present is a key discriminant for field personnel. At the same time, scattering strength (EMI “cross section”) depends markedly on type of metal or object shape, as well as volume. Therefore we generated the spheroidal mode coefficients for a population of single spheroids with random shapes, volumes, and metallic composition. Spheroids greater than a certain volume limit were identified as large while the rest were labeled as small. One collection of spheroids was used to train SVM while an independent set was used to validate the accuracy of the SVM classification. Notably, the magnitude of the scattered fields and corresponding scattering coefficients was largely unrelated to object size; nevertheless, the SVM classification in terms of volume for these synthetic objects was shown to be highly accurate. Furthermore, since UXO are often heterogeneous objects, we also generated the spheroidal coefficients from objects composed of two adjacent spheroids of random shape and volume and differing composition. We likewise trained and tested our SVM and were again able to produce predominantly correct classifications.

Environmental Effects on UWB Electromagnetic Induction Inversion Techniques and Forward Modeling of Unexploded Ordnance

B. J. Zhang

Massachusetts Institute of Technology, USA

K. O'Neill

Dartmouth College, USA

T. M. Grzegorzczak and J. A. Kong

Massachusetts Institute of Technology, USA

This project seeks to understand the effect of environmental factors on electromagnetic induction (EMI) measurements of unexploded ordnance (UXO) and the associated inversion techniques applied on the noisy measurements. The environmental factors include clutter, since UXO sites are highly contaminated with metallic clutter, and ground effects, because soil may be slightly permeable.

EMI measurements were taken of UXO overlaid by a surface dispersion of small metallic clutter pieces. Inversion was done to identify the UXO based on those noisy measurements. This was accomplished by optimizing the match between measured and modeled scattered magnetic fields, using a new generation of fast but accurate forward models. We used differential evolution (DE) to find the optimal match. Inversion is successful when the closest match originates from the correct UXO type out of the library of possible UXO types. For UXO obscured by clutter, it was shown that the inversion was successful for measurements which had signal-to-noise ratios up to 2.5 dB. Generally, a DE population size of at least 50 members and over 100 generations were necessary to achieve successful inversion from noisy measurements.

Furthermore, measurements were also taken of UXO buried in soil. Through analytical approximations of spheres embedded in permeable half-spaces, it was found that for the range of realistic soil permeabilities, all halfspace effects are negligible except for a magnitude offset in the real part of the measured frequency domain EMI signal. We incorporated this offset effect in our forward models and did optimization inversion on the measurements. The inversion was successful for UXO buried at shallow depths.

Lastly, clutter can be approximated as directional dipoles and their combined effect can be incorporated into our forward models along with the soil offset effect. Synthetic data was generated using this forward model. Our optimization inversion was successful using this synthetic data with 20 spheres randomly dispersed over an area of 0.7 by 0.7 meters. Furthermore, this improved forward model allows for Monte Carlo-type simulations to help understand the statistics of clutter noise and investigate ways of suppressing or filtering out that noise in measurements. Further research is also needed to enhance the robustness of our inversion techniques to overcome the environmental effects.

Analysis of Uniplanar Resonator Using a Wave Concept Iterative Method W.C.I.P.

N. Sboui, A. Gharsallah, and A. Gharbi
Faculté des Sciences de Tunis, Tunisia

H. Baudrand
ENSEEHIT, France

A global modeling of uniplanar resonator is presented. The analysis is achieved by using an iterative method based on the wave concept W.C.I.P.. Two techniques of excitations are used to initialize the iterative process. The analysis procedure is described, and S parameters show good agreement with published data. This approach is successfully applied to many problems for microwave and high speed integrated circuit CAD software.

The KMD EMS System in Chinese Continuous Casting

J. Li and Z. Q. Lai

Hunan Kemeid Mechanicsyco Ltd, China

J. H. Li and G. Q. Xie

GL Geophysical Laboratory, USA

The KMD electromagnetic stirrer (KM EMS) has widely applications in the Chinese continuous casting industrial. We installed KMD EMS for the continuous casting in almost 80% steel plant in the China. In this paper, we present our KMD EMS's applications in China. Recent, we used GLGEO_AGILD EMS modeling to simulate the magnetic field distribution in our KMD EMS stirring in the continuous casting. According the GLGEO_AGILD EMS simulation, we improve our KMD design and obtain more high quality stirring function and can reduce the cost for our stirring product. Many simulations show that GLGEO_AGILD is accurate and fast. The magnetic field movie by GLGEO_AGILD clearly shows that the rotational steel flow is driven by magnetic field. There are MEMS, SEMS, and FEMS installed in the strand. The AGILD can be used for associate simulation of the magnetic field caused by the multiple stirrings that will be important real time tool to monitor the steel and metal continuous casting processes. In the near future, we will use new GLGEO_AGILD EMS modeling to improve my real time control system and increase the efficiency of our KMD EMS. The GLGEO_AGILD EMS modeling is new Advanced Global Integral and Local Differential electromagnetic stirring software that is mode and patented by GL GEOPHYSICAL Laboratory [1, 2]. The GLGEO_AGILD EMS modeling challenges to FEM, FD, and Born like EM modeling for magnetic field in EMS. The GLGEO_AGILD EMS modeling has excellent advantages over FEM, FD, and Born like modeling.

REFERENCES

1. Xie, G. Q., J. H. Li, and F. Xie, "New global and local electromagnetic field modeling and inversion," *PIERS 2005*, Hangzhou, China, 2005.
2. Xie, G. Q., J. H. Li, and F. Xie, "Advanced GILD EM modeling and inversion," *Proceeding of PIERS 2005*, Hangzhou, China, 105–109, 2005.

A New Formulation for Scattering by Impedant 3D Bodies

B. Collard¹, B. Fares², and B. Souny¹

¹Ecole nationale de l'Aviation Civile, France

²Centre Europeen de Recherche et de Formation Avancee pour le Calcul Scientifique, France

Abstract—A new integral equation formulation is introduced for solving, in the frequency domain, the problem of electromagnetic scattering by an impedant (IBC) or perfect electric/magnetic (PEC/PMC) 3D body of arbitrary shape. It is based firstly, on a special application of the equivalence principle [2] where the 0-field exterior domain is filled with another impedant medium and, secondly, on the widely used PMCHW (Poggio, Miller, Chang, Harrington and Wu) formulation which forces field continuity through the scatterer surface [3]. Unlike other IBC formulations such as [4], this one also applies to PEC/PMC. Furthermore, in this last case, it appears to stabilize the numerical scheme in the vicinity of eigen frequencies. We will provide proofs and conditions of the wellposedness of the problem for impedant as well as for PEC/PMC bodies.

1. Introduction

Since the pioneering work of Leontovitch, Impedance Boundary Condition (IBC) has been widely used to simplify electromagnetic scattering problems. It simulates the material properties of a surface by forcing surface electric and magnetic fields to respect: $\mathbf{E}_{tan} = R\mathbf{n} \times \mathbf{H}_{tan}$, $R \in \mathbb{C}$ [1] where \mathbf{n} is the unit normal to the surface pointing into the outside of the impedant medium. It is absorbing when $Re(R) > 0$. Range of validity of IBC for imperfect conductors has been discussed in [1]. Many specific implementations have been surveyed, but only a few general numerical methods are available. The last ones are from Lange [5] and Bendali [4]. Beyond the algebraic approach, [5] appears to be very similar to the proposed new formulation. It mimics the widely used PMCHW (Poggio, Miller, Chang, Harrington and Wu) method [3] and introduces a specific parameter which behaves like an impedant “complement medium” whose impedance would be equal to the scatterer’s one. But, none of [5] and [4] methods extends to perfect electric (PEC) or magnetic (PMC) conductors. The proposed new formulation follows a more physical approach. It is based on a special application of the equivalence principle [2] where the 0-field exterior domain is filled with another impedant medium and on the use of the PMCHW technic. It does not require scatterer and complement domain impedances to be the same and, most of all, it extends to PEC and PMC bodies ($R_s \rightarrow 0$ or ∞).

This paper describes a way to generalize [5] formulation. Before posing the concerned integral equation system, we briefly remind how the initial problem is decomposed. The well posedness of the formulation is then demonstrated. Finally we give some numerical illustrations which validate this approach and point out its advantages.

2. Subproblem Decomposition

The equivalent principle [2] conduces to decompose any problem into several subproblems, each one being dedicated to a given portion of the original problem. Given a subproblem, we denote “active domain” the piece of problem extracted from the original one. The space surrounding an active domain is named “complement domain”. Fields are expected to be null there. 0 field being a Maxwell Equation solution whatever the medium within a source free domain, this allows to choose any medium for the complement domain. This property is often used to transform a subproblem into a free space problem by replacing a scatterer by free space. It is seldom used in other cases. The proposed formulation uses it twice: once, classically, in the first subproblem, by filling the scatterer volume with free space and, another time, in the second subproblem, by filling the complement domain with an impedant medium.

In order to illustrate this approach, let us consider a scatterer in free space lighted by a plane wave. We refer by D_S to the region of space embodying the scatterer. Its surface is denoted Γ . We refer by D_E (“exterior domain”) to the rest of the space interesting the problem. Normal vectors will always be supposed to be unit vectors pointing outside the specified domain: n_S and n_E pointing from D_S , respectively D_E , toward D_E , respectively D_S . The initial problem is decomposed into 2 subproblems as follow (Fig. 1):

PbE: the exterior problem. It includes: an active domain D_E containing free space, a complement domain CD_E filled with free space, a set of surface electric and magnetic fictive currents, respectively \mathbf{J}_E and \mathbf{M}_E on

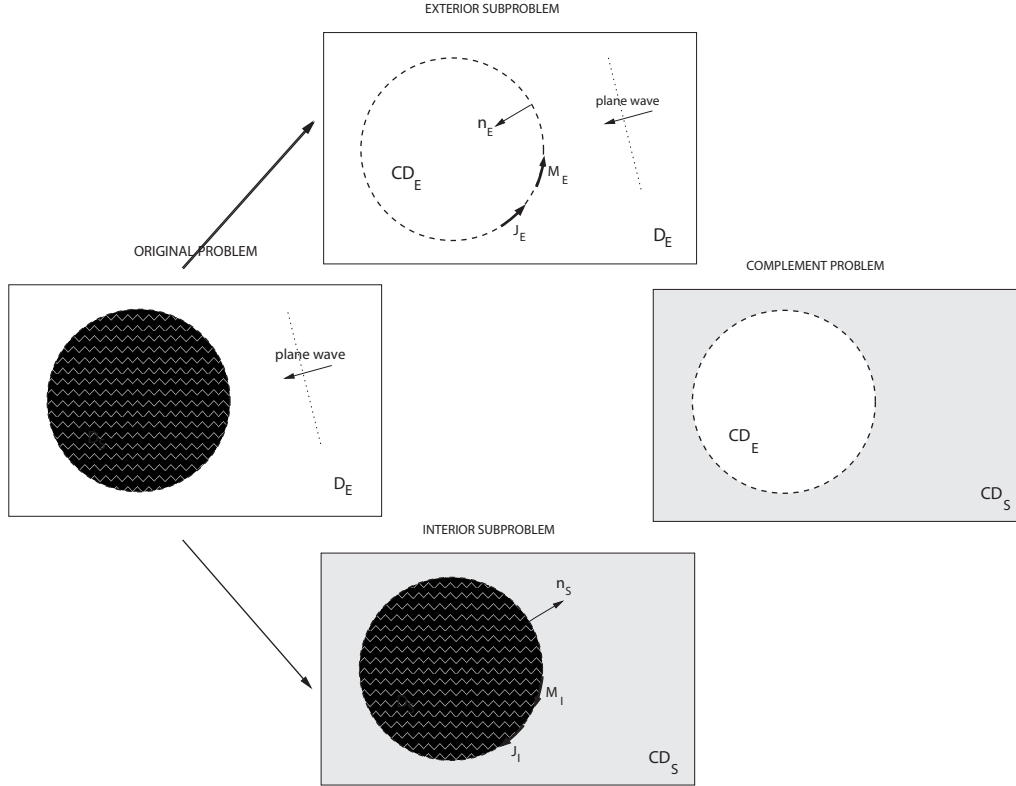


Figure 1: subproblems decomposition.

Γ , impressed sources generating a plane wave incident field. It is well known that this construction leads to a standard problem where fictive sources radiate in a free space environment.

PbI: the interior problem. It includes: an active domain D_S containing the impedant scatterer with local impedance R_s , a complement domain CD_S , filled with an impedant medium characterised by its local impedance R_c , a set of surface electric and magnetic fictive currents, respectively \mathbf{J}_I and \mathbf{M}_I on Γ , no impressed sources. Due to the complement choice, fields must satisfy an impedance boundary condition on both sides of interface Γ . On the scatterer side of Γ (point denoted x_s):

$$\mathbf{E}_{tan}(x_s) = R_s \mathbf{n}_S \times \mathbf{H}_{tan}(x_s) \quad (1)$$

On the complement side of Γ (point denoted x_{cs}):

$$\mathbf{E}_{tan}(x_{cs}) = -R_c \mathbf{n}_S \times \mathbf{H}_{tan}(x_{cs}) \quad (2)$$

3. Integral Equation Formulation

Once all subproblems posed, we evaluate, for each subproblem independantly, the scattered field on the active side of the interface radiated by fictive currents.

PbE radiating operators In a free space environment, fields radiated by surface currents are controlled by the familiar Stratton-Shu and jump relations on the interface. The field observed at point x_e on the D_E side of surface Γ is given by (Refer to [4] for expressions of Z and operators T and K):

$$\begin{aligned} \mathbf{E}_{tan}^{pbE}(x_e) &= \mathbf{E}_{tan}^{inc}(x) + ikZ(T\mathbf{J}_E)_{tan} + (K\mathbf{M}_E)_{tan} + \frac{1}{2}\mathbf{M}_E \times \mathbf{n}_E \\ \mathbf{H}_{tan}^{pbE}(x_e) &= \mathbf{H}_{tan}^{inc}(x) - (K\mathbf{J}_E)_{tan} + ikZ^{-1}(T\mathbf{M}_E)_{tan} - \frac{1}{2}\mathbf{J}_E \times \mathbf{n}_E \end{aligned}$$

PbI radiating operators A right combination of the usual boundary conditions [2] that links E and H fields on both side of a current sheet running on Γ

$$\begin{cases} \mathbf{E}_{tan}^{pbI}(x_s) = \mathbf{E}_{tan}^{pbI}(x_{cs}) + \mathbf{M}_I \times \mathbf{n}_S \\ \mathbf{H}_{tan}^{pbI}(x_{cs}) = \mathbf{H}_{tan}^{pbI}(x_s) + \mathbf{J}_I \times \mathbf{n}_S \end{cases} \quad (3)$$

and IBC relations (1) and (2) leads to the E and H field expression:

$$\begin{cases} \mathbf{E}_{tan}^{pbI}(x_s) = \frac{R_s}{R_c + R_s}(-R_c \mathbf{J}_I + \mathbf{M}_I \times \mathbf{n}_S) \\ \mathbf{H}_{tan}^{pbI}(x_s) = -\frac{R_c}{R_c + R_s}(\mathbf{J}_I \times \mathbf{n}_S + \frac{\mathbf{M}_I}{R_c}) \end{cases} \quad (4)$$

When the scatterer medium tends toward PEC ($R_s \rightarrow 0$), (4) reduces to:

$$\begin{cases} \mathbf{E}_{tan}^{pbI}(x_s) = 0 \\ \mathbf{H}_{tan}^{pbI}(x_s) = -\mathbf{J}_I \times \mathbf{n}_S - \frac{\mathbf{M}_I}{R_c} \end{cases}$$

Beyond there simplicity, they appear to be local operators, the numerical implementation of which does not require any long calculation and leads to a sparse matrix.

Connection— According to PMCHW, integral equations are built by forcing equality between surface fields associated to both subproblems:

$$\begin{cases} \mathbf{J}_I = -\mathbf{J}_E \\ \mathbf{M}_I = -\mathbf{M}_E \end{cases} \quad \text{and} \quad \begin{cases} \frac{R_s}{R_c + R_s}(-R_c \mathbf{J}_I + \mathbf{M}_I \times \mathbf{n}_S) = \mathbf{E}_{tan}^{inc}(x) + ikZ(T\mathbf{J}_E)_{tan} + (K\mathbf{M}_E)_{tan} + \frac{1}{2}\mathbf{M}_E \times \mathbf{n}_E \\ -\frac{R_c}{R_c + R_s}(\mathbf{J}_I \times \mathbf{n}_S + \frac{\mathbf{M}_I}{R_c}) = \mathbf{H}_{tan}^{inc}(x) - (K\mathbf{J}_E)_{tan} + ikZ^{-1}(TM\mathbf{E})_{tan} - \frac{1}{2}\mathbf{J}_E \times \mathbf{n}_E \end{cases} \quad (5)$$

4. Well Posedness

It worth pointing out that the formulation is not a strict application of the equivalence principle. In particular, nowhere it imposes 0 fields outside active domains. This fundamental characteristic must be proven independantly. In this intent, we define a new subproblem called ‘‘complement problem’’ PbC. It is built from the union of the complement domains of both subproblems, CD_E and CD_S plus their interface Γ .

According to the way subproblems are built, PbE and PbI solutions restricted to their respective complement domains CD_E and CD_S are solutions of the complement problem PbC:

$$\text{on } CD_S \text{ side } \begin{cases} \mathbf{E}_{tan}^{pbC}(x_{cs}) = \mathbf{E}_{tan}^{pbI}(x_{cs}) \\ \mathbf{H}_{tan}^{pbC}(x_{cs}) = \mathbf{H}_{tan}^{pbI}(x_{cs}) \end{cases} \quad \text{and on } CD_E \text{ side } \begin{cases} \mathbf{E}_{tan}^{pbC}(x_{ce}) = \mathbf{E}_{tan}^{pbE}(x_{ce}) \\ \mathbf{H}_{tan}^{pbC}(x_{ce}) = \mathbf{H}_{tan}^{pbE}(x_{ce}) \end{cases} .$$

Furthermore, PMCHW formulation forces equality between surface fields located into PbE and PbI active sides. By applying (3), one can easily prove that PMCHW formulation works as well with fields observed into the complement sides: $\begin{cases} \mathbf{E}_{tan}^{pbI}(x_{cs}) = \mathbf{E}_{tan}^{pbE}(x_{ce}) \\ \mathbf{H}_{tan}^{pbI}(x_{cs}) = \mathbf{H}_{tan}^{pbE}(x_{ce}) \end{cases}$. Consequently, in the Complement problem

$\begin{cases} \mathbf{E}_{tan}^{pbC}(x_{cs}) = \mathbf{E}_{tan}^{pbC}(x_{ce}) \\ \mathbf{H}_{tan}^{pbC}(x_{cs}) = \mathbf{H}_{tan}^{pbC}(x_{ce}) \end{cases}$, tangential components of field are continuous through Γ and, finally, PbC appears to be a source free problem. AS FAR AS IT IS NOT A SINGULAR PROBLEM subject to eigen modes, its unique solution is ZERO. This proves that field solutions are equal to 0 in all complement domains whatever the subproblem.

Consequently, PbI and PbE solutions are the same as the ones provided by the equivalence principle, combination of which is known to be the unique solution of the original problem.

Finally, we can conclude that the well posedness condition requires that *the problem built on the complement domains union is a non singular problem.*

5. Numerical illustrations

Numerical results obtained with a unit sphere meshed with planar triangles (750 edges) confirm the formulation validity and advantages. Equivalent currents and test functions are expanded using RWG elements [6].

- **Accuracy:** in the case of an IBC sphere ($R_s = 100$), we have compared numerical results obtained from three formulations: the new formulation, CERFACS implementation of Leontovitch problem [4] and Mie series with boundary condition (1) imposed at the sphere surface [2]. The sphere is lighted from the bottom (+z direction) by a x-polarised plane wave which wave number is set to $k = 2$. Complement medium impedance is $R_c = 2$. Fig. 2 reports the radar cross section (RCS) observed in different direction using the 3 methods. Angle 0 corresponds to the direction of incidence. The 3 resulting curves are in perfect agreement. New formulation and CERFACS RCS results are strictly superimposed. This visual feeling is confirmed by the relative errors values on equivalent currents computed via the 3 methods (see Tab. 1).
- **Numerical stabilization:** the behaviour of one selected RWG current element of a PEC sphere ($R_s = 0$) has been followed when wave number k varies in the vicinity of the first eigenfrequency of the spherical

cavity: $k_e = 2,76$. In this case, we use edge excitation by turning on edge 1 (excitation vector set to $[1 \ 0 \ 0 \ \dots \ 0 \ 0]$). Fig. 3 reports real and imaginary parts of the observed flux as a function of k when EFIE or proposed formulation is used. One can easily notice that the resonance peak, that clearly appears with EFIE, is suppressed by the new method. The proposed formulation is thus no subject to spurious solutions when $R_s \rightarrow 0$ or ∞ .

Table 1: Equivalent current relative error.

degree of freedom	formulations	error
electric	Cerfacs / New formulation	1,6%
electric	New formulation/ Mie	1,7%
magnetic	New formulation / Mie	1,6%

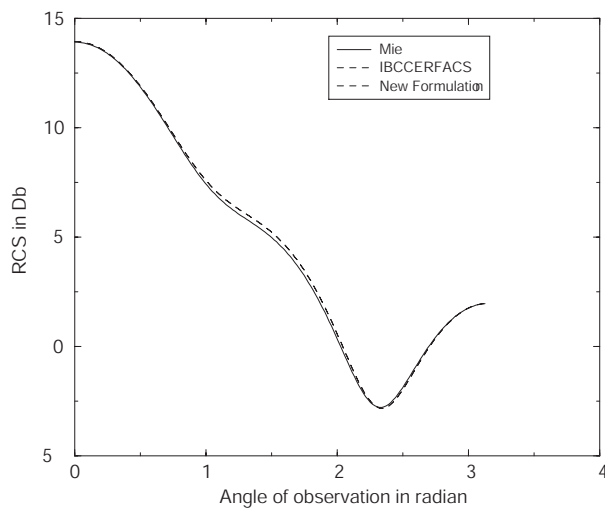


Figure 2: RCS obtained by 3 methods.

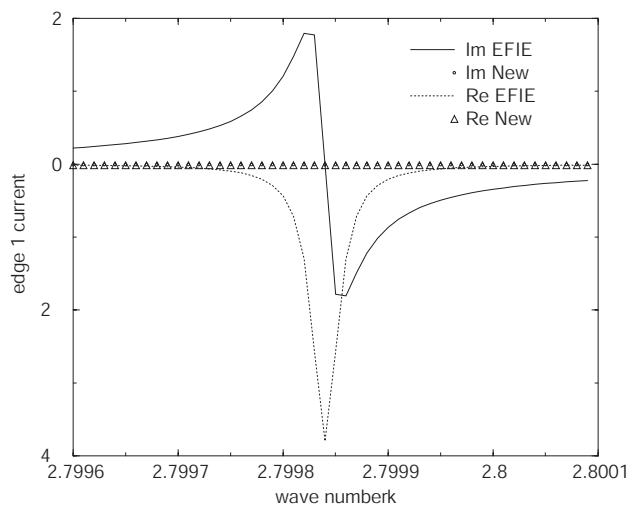


Figure 3: Real and imaginary part of current value computed by EFIE and new formulation.

4. Conclusion

The proposed formulation provides practitioners in computational electromagnetism with a general well posed method to deal with all kinds of impedant bodies, from usual IBC medium up to very good and even perfect conductors without any risk of spurious solution. Interior problem local operators are very easy to implement using RWG elements. They generate a negligible extra computation compared to the one needed for the exterior problem. Since magnetic currents must always be taken into account, even for PEC/PMC, the main drawback is the doubling of the number of degrees of freedom compared to [4]. In addition, it worth noting that the well posedness condition which states that the complement problem must be non singular could be extended to all forms of PMCHW formulations.

REFERENCES

1. Wang, D. S., "Limits and validity of the impedance boundary condition on penetrable surfaces," *IEEE trans. Ant. Prop.*, Vol. 35, 453–457, Oct. 1987.
2. Harrington, R. F., *Time Harmonic Electromagnetic Fields*, Mac Graw Hill, 1961.
3. Poggio, A. J. and E. K. Miller, *Computer Techniques for Electromagnetics*, Oxford, U. K. permagon, 1973.
4. Bendali, A., M'B. Fares, and J. Gay, "A boundary-element solution of the leontovitch problem," *IEEE Trans. Ant. Prop.*, Vol. 47, 1597–1605, Oct. 1999.
5. Lange, V., *Equations Integrales Espace-Temps Pour Les Equations De Maxwell. Calcul Du Champ Diffracte Par Un Obstacle Dissipatif*, PhD dissertation, Univ Bordeaux I, France, 1995.
6. Rao, S. M., D. R. Wilton, and A. W. Glisson, "Electromagnetic scattering by surface of arbitrary shape," *IEEE Trans. Ant. Prop.*, Vol. 30, 409–418, may 1982.

